SUPPLEMENTARY MATERIAL

1. X-ray CT of 30 mango fruit & geometrical shape description of mango fruit 2.

The average shape and size of a mango fruit of the cultivar Kent were extracted. To this end, a geometrical model generator for horticultural products was used [58,59]. This generator starts from non-destructive imaging of multiple fruit and uses this information for geometrical shape description.

First, X-ray CT was used to obtain the three-dimensional size and shape of the outer geometry of the fruit and the internal features (seed). In this study, 30 Kent mangos were scanned, which were purchased from an importer (Starfruit Company, Brussels, Belgium) that delivered the fruit by airfreight from Ethiopia. The fruit in this study were scanned with a medical scanner (Somatom, Siemens Medical Solutions Inc, Hoffman Estates, IL), which is a fast imaging instrument that still provides a sufficient resolution for the present application (voxel size: 977 x 977 x 600 µm). To this end, fruits were put in crates in a regular pattern, separated by styrofoam boards to assure that individual fruit could be easily segmented in the acquired 3D X-ray image. Next, Otsu grey scale thresholding and edge detection were used to extract the 3D surface contour of the outer surface and edge of the seeds for each fruit from the scans using Matlab. With this digital shape information of a batch of fruit, a statistical shape description based on Fourier descriptors was performed [58,59]. As a result, the average outer surface contour of the fruit was determined. The surface contour of the seed was determined in a more simplified way, by approximating it as an ellipsoid, based on the average volume of the seeds and their dimensions. From this geometrical information, a 3D CAD model of the mango fruit and seed (.IGES) was generated, which has the average shape and size of a Kent mango. The peel was not included in the model, as its impact on the cooling kinetics is limited. The reason is that it is rather thin and its thermal properties are in the same order of magnitude as of the fruit pulp.

2. X-ray imaging of artificial mango fruit

To visualize and characterize the internal components of the artificial fruit, an X-ray computed tomography was performed. Radiographs were made by rotating the object in discrete steps of 0.25 degrees over an angle of 360 degrees. By reconstruction of the 2D radiographic images taken under different view angles using an X-ray source and detector, a 3D image of the artificial fruit was obtained. The different components of the artificial fruit could be identified, including shell and thermal filling, based on differences in attenuation properties of the materials. The X-ray CT scans were made on a micro CT setup consisting of an X-ray tube (XT9160-TXD, Viscom, Hannover, Germany), a high precision rotation table (UPR-160F AIR, Micos, Dübendorf, Switzerland) and a flat panel detector (XRD-1621-CN3ES, Perkin Elmer, Waltham, United States). The scans were performed at 150 kV and 66 µA, with a field of view of 20.8 x 4.9 cm^2 and a pixel resolution of 103 µm. The images were segmented for further analysis using the commercial software Avizo (Edition 9.5, Thermo Fisher Scientific, Waltham, USA).

3. Heat of respiration and mass loss of mango fruit

The source term (Eq.(1)) which accounts for the heat of respiration in the fruit pulp [W m_{pulp}^{-3}] in our multiphysics model is defined as:

$$Q_s = \rho_p S_p \tag{S1}$$

where subscript p indicates fruit pulp, ρ_p is the density of the fruit pulp [kg_p m_p^{-3}], and S_p is the mass-based heat of respiration [W kg_p^{-1}]. Mangos are strongly respiring fruit, with respiration heats of 83 mW kg_f^{-1} at 10 °C up to 340 mW kg_f^{-1} at 20 °C [35,38], where subscript f indicates the entire fruit (pulp and seed). We took this literature data to determine respiration heat as a function of temperature, by linear interpolation. For values above 20 °C and below 10 °C, a constant-value extrapolation was used (Figure S1).

The values from literature (S_f) are based on measurements on entire mango fruit, so these are defined in W kg$_f^{-1}$. In reality and in our multiphysics model, only the fruit pulp is respiring, however. As such, the respiration heat data from literature needed to be corrected to obtain the values (S_p in Eq.(S1)) in W kg$_p^{-1}$, which will be slightly higher. Following correction was applied for this purpose:

$$S_p[\frac{W}{kg_p}] = S_f[\frac{W}{kg_f}] . \frac{m_f}{m_p}[\frac{kg_f}{kg_p}]$$
(S2)

The correction factor ($CF=m_f/m_p$) in this study was 1.053, which means a 5% difference. Both respiration heats (S_f and S_p) are presented in Figure S1, together with the data from the literature. For our mango fruit (0.474 kg), this implies the respiration heat (S_p) varies between 41 – 170 mW.

The mass loss from mango fruit in overseas cold chains by ship over several weeks is rather limited. Typically, about 5 % is found at optimal storage temperature and humidity, where a maximum of 7-9% is acceptable for the fruit to be still viable for sale [18]. This mass loss needs to be limited to avoid shriveling, which is why mangos are stored at elevated humidity levels. A mass loss of 5% in weight over 20 days would induce an evaporative cooling load below 35 mW for our fruit in a refrigerated state. This heat load is even lower than respiration heat production. Therefore, the latent heat of evaporation due to mass loss is not included.
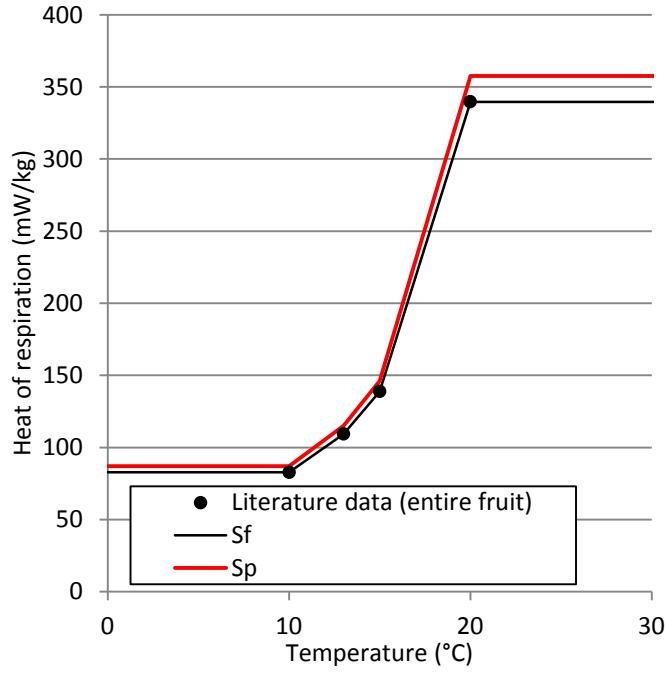
Figure S1. The heat of respiration from the literature [38] *and interpolated functions for the entire fruit (S$_f$) and rescaled, so the respiratory heat production only occurs in the fruit pulp (S$_p$).*

4. Model for temperature-dependent quality attribute evolution

The quality attribute data was taken from literature for physiologically mature mangos [43]. Here, data were reported on firmness (Firm), soluble solids content (SSC), titratable acidity (TA), vitamin C (vitC) and beta carotene (BC) at two different temperatures (10 °C and 25 °C) for the mango cultivar 'Apple'. The order of the reaction was chosen based on the best fit of the model with the data or the inherent order of the decay reaction (e.g., vitamin loss is a first-order reaction), although often little differences were present between first- and zero-order approximations. Depending on the order of the reaction, the constant $k_{0,j}$ [s^{-1}] and activation energy $E_{a,j}$ [J mol^{-1}] were determined as follows. First, the rate constants were determined at both temperatures, namely $k_j(10°C)$ and $k_j(25°C)$, based on Eqs. (6-7) for a zero- and first-order reaction:

$$k_j^{O(0)}(T) = \frac{A_{0,j} - A_j(t_{end})}{t_{end}} \tag{S3}$$

4

$$k_j^{O(1)}(T) = -\frac{1}{t_{end}} \ln\left(\frac{A_j(t_{end}) - C_j}{A_{0,j}}\right) \tag{S4}$$

where t_{end} is the time when the quality attribute was measured last. Using this information, the Q_{15}

value was determined for each quality attribute. It is the ratio of the rate constants at temperature T

and T+15K:

$$Q_{15} = \frac{k_{i,T+15}}{k_{i,T}} \tag{S5}$$

Out of the Q_{15} value, the activation energy was extracted, assuming $k_{0,j}$ is constant:

$$Q_{15} = \frac{k_{0,j} e^{\frac{-E_{a,j}}{R(T+15)}}}{k_{0,j} e^{\frac{-E_{a,j}}{RT}}} = \frac{e^{\frac{-E_{a,j}}{R(T+15)}}}{e^{\frac{-E_{a,j}}{RT}}} \tag{S6}$$

$$\ln(Q_{15}) = \frac{-E_{a,j}}{R(T+15)} - \frac{-E_{a,j}}{RT} = \frac{-E_{a,j}T + E_{a,j}(T+15)}{RT(T+15)} = \frac{15E_{a,j}}{RT(T+15)} \approx \frac{15E_{a,j}}{RT^2} \tag{S7}$$

$$E_{a,j} \approx \frac{RT^2}{15} \ln(Q_{15}) \tag{S8}$$

From Eq.(S8) and Eq.(8), the constant $k_{0,j}$ was extracted:

$$k_{0,j} = \frac{k_j(T_{cal})}{e^{\frac{-E_{a,j}}{RT_{cal}}}} \tag{S9}$$

This constant needed to be calibrated at a certain temperature T_{cal}, as slight variation will occur and

the value is not entirely constant. In this study, T_{cal} = 25 + 273.15 K was chosen, which leads to an exact

match of the final quality attribute with the data at 25 °C, but a small discrepancy with the data at 10

°C. We preferred to calibrate with the high-temperature dataset, as the decay processes occur much

faster here, so it is more critical that they are captured most accurately. The model and experimental

data at two temperatures are shown in Figure 8 for all attributes, indicating a good agreement at both temperatures. The model parameters are specified in Table 3 for each quality attribute.

In addition to these individual quality attributes, the overall fruit quality (A_{sl}), which is linked to the remaining storage life (SL), was also modeled using a first-order model. Following assumptions were applied, based on information in the literature on various mango cultivars [18,43,60,61]: (1) mango fruit can be stored for approximately 28 d or 7 d (t_{end}) at 12 °C for mature green (MG) and tree-ripe (TR) mangos, respectively. This implies A_{sl}(12 °C, 0 hours) = 100% = $A_{0,sl}$ and $A_{end,sl}$(12 °C, t_{end} = 28 d for MR or 7 d for TR) = 1%, so when the fruit is considered to be lost; (3) An increase in temperature of 10 °C triples the rate constant or decreases storage life with a factor 3. This result means that the Q_{10} value = 3. This Q_{10} value equals the ratio of the rate constants at temperatures T and T+10K (=k_{T+10}/k_T) and is typically about 2-3 for degradation reactions in fruit [4,5]. Note that these values are dependent on the cultivar, harvest location, and exact classification of the ripeness. However, the purpose of this study was to identify differences between treatments for mango fruit. As such, the conclusions will remain the same, even if slightly different values are taken for t_{end} or Q_{10}. Based on the relations above between these parameters, the constant $k_{0,j}$ and activation energy $E_{a,j}$ were determined for mature green and tree-ripe mangos (Table 3). The temperature dependency of this overall quality decay is shown in Figure S2.
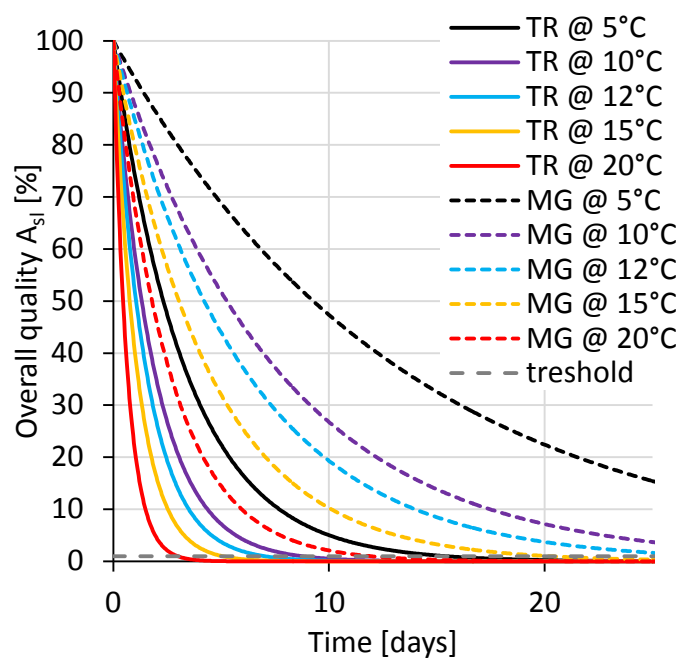
Figure S2. The overall quality of tree-ripe and mature-green mangos as a function of storage temperature and time. The threshold value, where quality is considered to be fully lost (1%), is shown by the dashed grey line.

5. Verification of the thermophysical model

The performance of the finite element model to accurately predict the cooling of solid products, such as fruit, is verified by comparison with empirical data from [48] for a sphere with radius R [m]. Here, the unsteady state heat conduction process (i.e., cooling) is represented using the temperature ratio T^* as a function of the Fourier number (Fo):

$$Fo = \frac{\alpha t}{R^2} \tag{S10}$$

$$T^* = \frac{T_f(r) - T_{ref}}{T_{f,0} - T_{ref}} \tag{S11}$$

where α is the thermal diffusivity of the fruit ($\alpha = \lambda_f/(\rho_f c_{p,f})$) [m^2 s^{-1}], t is the time [s], subscripts *f,0 and ref* represent the initial temperature of the fruit and the setpoint temperature of the air. $T_f(r)$ represents the fruit temperature at a distance r from the center of the sphere. The relation *T*-Fo* relation is given as a function of the parameter m, which is defined as:

$$m = \frac{\lambda_f}{h_{c,T} R} \tag{S12}$$

where $h_{c,T}$ is the convective heat transfer coefficient (CHTC [W m^{-2} K^{-1}]), and λ_f is the thermal conductivity of the fruit [w m^{-1} K^{-1}]. In this paper, simulations were performed for $m = 0.5$ for a temperature difference $T_{f,0}$-T_{ref} of 10 °C. The equivalent sphere diameter of Table 1 was used, together with the thermal properties of the fruit pulp (Table 2). The resulting CHTC for the simulations via Eq.(S12) was 18.0 [W m^{-2} K^{-1}]. The comparison of empirical data and simulations is given in Figure S3, showing the temperature ratio T^* as a function of the Fourier number, for the temperature at the spherical fruit surface ($r=R$) and inside its core ($r=0$). The very good agreement of empirical and simulation data indicate the accuracy of the implemented model.
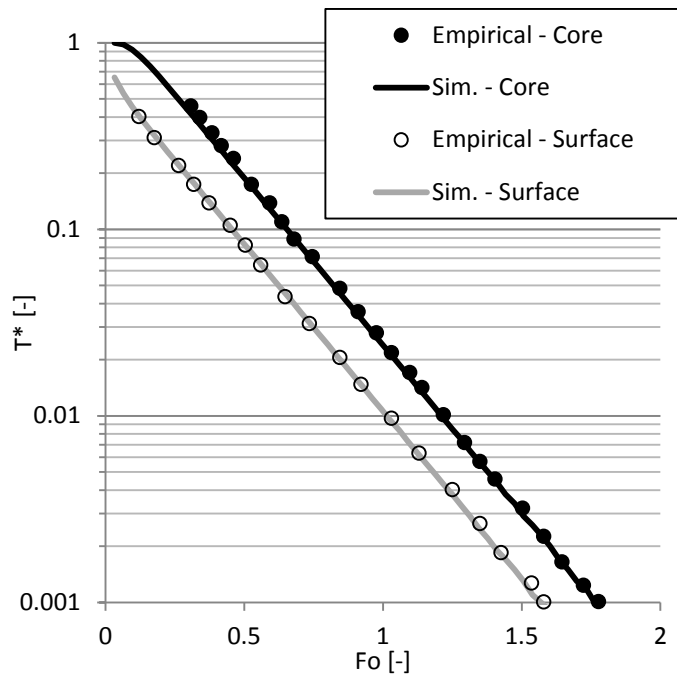
Figure S3. Temperature ratio T* (logarithmic scale) as a function of the Fourier number, for the temperature at the spherical fruit surface (r=R) and inside its core (r=0) for the simulations and empirical data.

6. Measurements of air temperatures in actual cold chains

In several commercial shipments from South America (Peru for airfreight, Brazil for maritime transport, performed in period 01.2018-04.2018) to Switzerland, air temperature sensors were installed during loading of the cargo at the exporter and were retrieved again at the importer. This data provides realistic temperature data for the overseas cold chain. For this purpose, XSense® HiTag2™ temperature data loggers were used, which have an accuracy of ± 0.5 °C and sampled temperatures every 10 minutes.

7. Climate chamber experiments

The climatic chamber (Feutron Klimasimulation GmbH, Feutron KPK 800) has inner dimensions of 770 × 1380 × 745 mm, so an inner volume of 800 L. Air is supplied from the bottom via a perforated plate and is extracted at the top of the chamber. The temperature range is −40 to 100 °C ± 0.2 °C, the relative humidity range is 10–95% ±3%, and the airspeed is about 0.3-0.4 m s^{-1}.

Five mango fruit (cv. *Kent*) were purchased at a local retailer. The individual fruit was selected to have a weight that was as close as possible (445 g with a standard deviation of 6g) to that of the simulated fruit (474 g). Also, an artificial mango fruit was manufactured according to the method of [49] (Figure 4). This artificial fruit is biomimetically designed to have the same shape, size, and thermal properties as an average Kent mango. Note that the resulting weight of the artificial fruit was 448 g. By using the same 3D CAD model (Figure 1), the numerical model could be given the same geometrical and thermal properties as the artificial fruit so that a clear comparison can be made.

The artificial fruit and the five real mango fruit were each equipped with an iButton® temperature sensor in the core, so the interface between the seed and the pulp along the primary axis (Figure 1 (probe 2) and 4). In the artificial fruit, a sensor was also placed in the enclosure at its surface. The temperature sensor was inserted in the mango fruit by making an incision. Before the experiment, all fruits were stabilized in another climatic room to 20.3 °C. Afterward, the fruits were placed in the climatic chamber, which ran at 2.8 °C, and a cooling period of 6 hours was monitored. Subsequently, the fruits were placed in another climatic chamber, which ran at 20.4 °C, where the fruit was heated back up. Finally, the fruit were placed back in the climatic chamber, which ran at 2.8 °C, and a cooling period of 10 hours was monitored. The results of these two cooling runs are reported. Note that this low temperature of 2.8 °C is typically too low for mango fruit cold storage, but was chosen so low to have a larger temperature range, while still being above the freezing point.

Although the overall airspeed was measured with an anemometer, this airspeed could not be used to determine a reliable CHTC with the correlations reported (Eq. (3-4)). The reasons are that:

- The airflow field and the turbulence level are different from those which were used to determine the correlations, which were usually determined for low-turbulent flow in a wind tunnel. These differences arecaused by the perforated plate via which the air enters the chamber, which is located near the bottom. As such, the air velocity profile (in an empty chamber) is not necessarily uniform and was difficult to measure univocally. Furthermore, the turbulence level in the chamber will be higher, which can significantly enhance the magnitude of the CHTC.

- There were bars present on which the fruit was laid. Similarly, these bars will induce a different, non-uniform airflow field around the fruit and will lead locally to higher airspeeds.

- A blockage of the airflow is generated by the bars and the mango fruit which is placed in the climatic chamber. Due to this blockage, a local speed-up of the air will occur around the fruit, which will enhance the CHTC. This blockage ratio in the experiment was estimated to be about 30%.

As a result, the use of the correlations (Eq. (3-4)) at the measured airspeed of 0.3-0.4 m s^{-1} provided lower cooling rates than those measured experimentally. As the accuracy of the thermophysical model was verified, this mismatch between simulations and experiments originates from a mismatch in predicted and actual CHTC. Therefore, an inverse determination of the CHTC was done for the simulations, based on the data. The resulting CHTC was 19 W m^{-2}K^{-1}. If one relies on the CHTC correlation for the ellipsoid (Eq. (4)), assuming airflow is parallel to the long side of the mango fruit, this would imply an equivalent airspeed of about 1.6 m s^{-1}. For the reasons mentioned above, this correlation is not valid for the flow conditions in the climatic chamber.

8. Grid sensitivity analysis

An appropriate grid was constructed for the (half) mango fruit, based on a grid sensitivity analysis. For this grid sensitivity analysis, three different grids were evaluated, namely a fine, base, and coarse grid with 114'795, 9'441, and 671 finite elements. A gradual refinement toward the air–fruit and pulp–seed interfaces was applied to enhance numerical accuracy and stability, as the largest gradients occur there, particularly at the start of the cooling process.The differences with the fine grid are depicted in Figure S4 for the base and coarse grid for the fruit core temperature (Probe 2 in Figure 1) and the fruit surface temperature (Probe 3 in Figure 1) It is clear that even for the coarse grid, the differences with the fine grid are very limited. The base grid, which is the one used in the present study, has a spatial discretization error on the local fruit surface and pulp temperatures that is below 0.01 °C. The grid consists of 9'441 tetrahedral and prismatic finite elements.
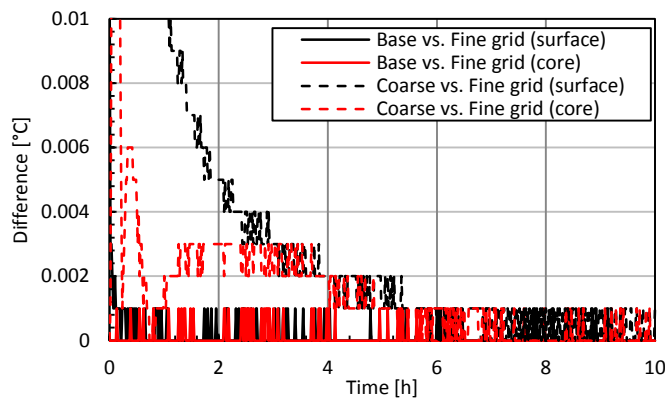

Figure S4. The difference in temperature of the base and coarse grid with the fine grid as a function of time for the temperature at the surface and the fruit pulp core.